



A two-wheeled inverted pendulum robot with friction compensation



Fuquan Dai^a, Xueshan Gao^{b,c,*}, Shigong Jiang^{b,c}, Wenzeng Guo^b, Yubai Liu^b

^a School of Mechanical and Automotive Engineering, Fujian University of Technology, Fuzhou, China

^b Department of Mechatronics Engineering, Beijing Institute of Technology, Beijing, China

^c State Key Laboratory of Robotics and System (Harbin Institute of Technology), Harbin, China

ARTICLE INFO

Article history:

Received 8 April 2014

Accepted 21 June 2015

Available online 4 July 2015

Keywords:

Friction compensation

Friction parameter determination

Sensor data fusion

Sliding mode control

Two-wheel inverted pendulum

ABSTRACT

This paper introduces a method of design and implementation of a two-wheeled inverted pendulum (TWIP) robot with friction compensation. Friction in the drive mechanism is a critical factor of robot self-balancing and affects its performance. The friction parameters are identified based on the dynamic model of the drive mechanism. The dynamics of the whole robot system are obtained by the Lagrangian function method and take the robot drive mechanism friction into account. Sliding mode controllers for self-balancing and yaw motion are designed independently, although the TWIP robot is coupled as a nonlinear system. A low cost but low accuracy gyro and accelerator in consumer electronics grade is adopted to estimate the pitch angle and pitch rate. Using the sensor data from the gyro and accelerator fused with the help of a Kalman filter, the robot body pitch angle is obtained precisely, and these are the key state variables for TWIP control. The effect on the sensor installation location is analysed and corrected with innovation, and the precision of the pose estimation is improved accordingly. Several physical experiments are conducted, and the results demonstrate that the proposed method is effective.

© 2015 Elsevier Ltd. All rights reserved.

1. Introduction

A two-wheeled inverted pendulum (TWIP) robot has become a research hotspot in the past decades because of advantages such as a small footprint, zero radius turning ability, and its agility in narrow spaces and crowded conditions. Recently, a TWIP robot has become a good choice as a city commuting or patrol transporter, such as Segway, because of more and more serious city traffic congestion. A TWIP robot can also be chosen as the service robot platform because of manoeuvrability and taking up less space, such as Anybots QB [1]. Furthermore, a TWIP robot is an under-actuated nonlinear system, which makes it a prospective robot as an educational device for teaching or a research platform for testing advanced control methods [2–4].

Various control methods were proposed to regulate the TWIP robot because this type of robot is challenging to control due to its under-actuated and nonlinear characteristics. PID is the most common control method for TWIP robot control, as there is no need to build the mathematics model but only to choose the parameters by trial and error or by experience [3,5,6]. However,

PID cannot reach satisfactory control effects when disturbance and modelling inaccuracy exist. Two decoupled state space controllers were adopted in JOE [7]: one for balance (pitch movement) and the other for turning (yaw movement). This method is based on the linearised dynamic model obtained by Newton's analysis method and decoupled from pitch and yaw movements. LQR is also widely used for this type of robot [8], which is also based on the dynamic model of the robot. Considering model uncertainties such as parameter uncertainties and external disturbances, a sliding control method was proposed for robust velocity control [9]. A fuzzy control method was adopted in TWIP control in [10–12]. Other intelligent control methods and robust control methods have also been reported in TWIP control, such as a neural network [13], a cerebellar-model articulation controller [14], backstepping [15], H_∞ [16], and adaptive control [17].

Much research focuses on improving posture measurement because precise posture measurement is the foundation of TWIP robot balance control. Unlike a conventional inverted pendulum, a TWIP robot cannot adopt an encoder and other sensors in a relative angle measurement, as the pitch angle of the TWIP robot that needs to be obtained is an absolute angle between the robot body and the horizontal plane. To solve this issue, accelerometers and gyros are widely used to measure the angle and angle rate of a TWIP [18,19]. Because of gyro drift and the accelerometer being easily affected by vibration, a Kalman filter and a complementary filter were designed to fuse sensing data from an accelerometer

* Corresponding author at: School of Mechanical and Automotive Engineering, Fujian University of Technology, No. 3 Xueyuan Road, University Town, Minhou, Fuzhou 350118, China. Tel.: +86 0591 22863232.

E-mail addresses: fuquan_dai@163.com (F. Dai), xueshan.gao@bit.edu.cn (X. Gao).

Nomenclature

$\frac{d^n}{dt^n} \mathbf{x}$	time derivative of vector \mathbf{x} with respect to frame n	R, L, W	radius of the wheel, distance between the body and wheel, and width of the body
$\frac{\partial F}{\partial \mathbf{x}}$	partial derivative of a function of F with respect to \mathbf{x}	m_w, M	mass of the wheel and mass of the robot body
$\text{sgn}(\cdot)$	sign function	i, v	motor current and motor voltage
l, r, b	subscripts indicating left or right wheels and the robot body, respectively	L_m, R_m, K_t, K_b	terminal inductance, terminal resistance, torque constant, and back electromotive constant of the DC motor, respectively
T_f, T_c, T_s, T_m	total friction torque, coulomb friction torque, the static friction torque and the torque produced by the motor	θ, ϕ	rotary angle of the wheel θ and yaw angle of the robot
σ, σ_2	viscous friction coefficient in the Coulomb plus viscous friction model, and the viscous friction coefficient in the Stribeck friction model	$\psi, \dot{\psi}, \psi_k, \psi_{k+1}$	pitch angle, pitch angle rate, pitch angle value in the k th sample period, and pitch angle value in the $(k+1)$ th sample period
ω	rotating velocity of the wheel	$\dot{x}, \dot{y}, \dot{z}$	velocity along the x, y and z axes
v_s	Stribeck velocity	L_a	Lagrangian function
n	reduction ratio of the gear box.	T_1, T_2, U	translational kinetic energy, rotational kinetic energy, and potential energy of the robot, respectively
$J_m, J_w, J_{\text{redu}}, J_\psi, J_\phi$	rotary inertia of the motor, rotary inertia of the wheel, rotary inertia equivalent to the motor shaft, robot rotary inertia about the x axis, and robot rotary inertia about the z axis	Δ_1, Δ_2	parameter uncertainty

and a gyro [18,20]. Furthermore, a Segway was equipped with 5 accelerometers and 2 gyros redundantly for safety [21]. However, there are still some problems to solve to obtain the precise posture. Conventional accelerometers and gyros are too expensive for many application situations, so low cost and low accuracy MEMS (micro-electro-mechanical systems) sensors common in consumer electronics are chosen in this paper. The accelerometer obtained the pitch angle by measuring the gravitational acceleration projected on the axis, and the axis is fixed on the accelerometer. As a result, it is easily disturbed by other sources of acceleration such as vibration and rotation of the robot body. This paper proposes a novel method to eliminate the influence of rotation of the robot body by combining the output with the gyro.

The friction of the TWIP robot transmission mechanism is seldom studied in the literature, but it is an important factor of the TWIP robot performance. Friction is a highly nonlinear phenomenon between two contacting surfaces and causes steady state errors, limit cycles, and poor performance [22]. Friction identification and compensation have been widely studied in the past based on static or dynamic models [23–28]. To improve the performance of the TWIP robot, the friction model of the transmission mechanism is built according to the robot parameters identified in this paper. Friction is then compensated for in the control because the friction model is obtained, which evidently improves the state error in balance control.

The main contributions of this paper are as follows.

- (1) Parameters of the TWIP robot are identified using a simple and effective method.
- (2) Compared with the balance controller without friction compensation, the proposed controller with friction compensation can improve the steady state error effectively (approximately 2–3°) and has no crawling phenomenon. Furthermore, compared with the classical PID controller, overshooting is obviously smaller, even though the initial pitch angle is nearly 30°. In consequence, the balancing control performance is improved with the proposed method.
- (3) Good posture sensing is implemented using low cost sensors and considering the sensor installation site.

The paper is organized as follows. Some critical parameters, including the friction parameters and the equivalent moment of inertia, are introduced in Section 2. The dynamic model of the

robot is built based on the Lagrangian function method in the next section. Section 4 introduces the sensor data fusion considering the installation site. In Section 5, a sliding mode controller is designed on the basis of the dynamic model, and physical experiments are conducted to validate the design of the robot.

2. Parameter identification

The overview of the TWIP is shown in Fig. 1, which consists of two wheels and one body. The two wheels are directly connected to the output shaft of the DC brushed motors, and the wheels are placed on the same axis. A box is fixed on the base of the robot body, and a weight of 0.5 kg is placed in the box as a test load.

To construct a precise dynamic model of the TWIP, which is important to achieve the desired control performance, the parameters of the robot are identified before the mathematical derivation. Many robot parameters can be measured directly or found in product manuals, such as the radius of the robot wheels, the mass of the robot's constituent parts and the characteristics of the DC motors, or can be obtained by simple calculations, such as the centre of gravity (CG) of the robot body. However, some parameters of the robot are difficult to determine, especially the friction

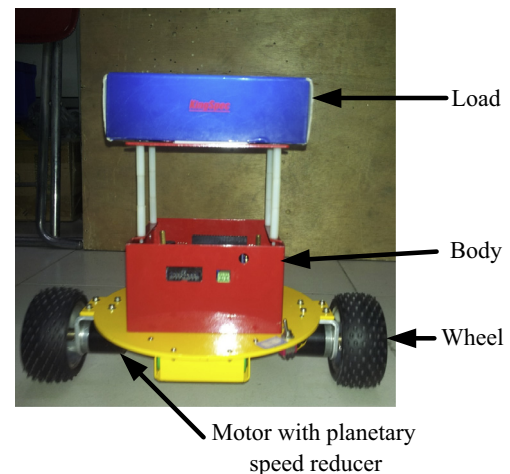


Fig. 1. Overview of the TWIP.

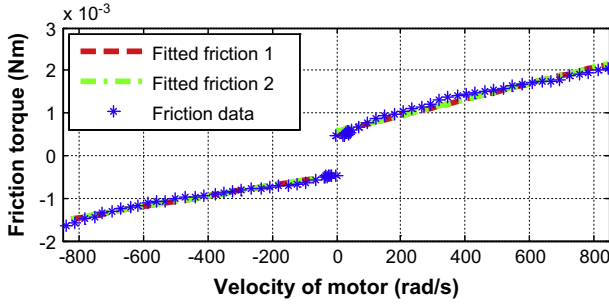


Fig. 2. Friction of the left drive mechanism. The blue asterisk line denotes the raw friction data; the green dashed line denotes the friction fitted by the friction model including Coulomb plus viscous friction; and the red dashed line denotes the friction fitted by the Stribeck friction model. (For interpretation of the references to colour in this figure legend, the reader is referred to the web version of this article.)

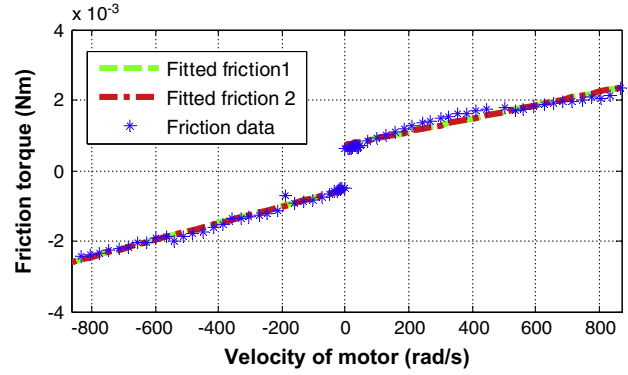


Fig. 3. Friction of the right drive mechanism. The blue asterisk line denotes the raw friction data; the green dashed line denotes the friction fitted by the friction model including Coulomb plus viscous friction; and the red dashed line denotes the friction fitted by the Stribeck friction model. (For interpretation of the references to colour in this figure legend, the reader is referred to the web version of this article.)

Table 1
Coulomb plus viscous friction model parameters of the left drive mechanism.

Friction parameters	When velocity is positive	When velocity is negative	Unit
T_c	-7.223×10^{-4}	-5.333×10^{-4}	Nm
σ	1.886×10^{-6}	2.394×10^{-6}	Nm/(rad/s)

Table 2
Stribeck friction model parameters of the left drive mechanism.

Friction parameters	When velocity is positive	When velocity is negative	Unit
T_c	-7.272×10^{-4}	-5.44×10^{-4}	Nm
T_s	-6.301×10^{-4}	-4.832×10^{-4}	Nm
ν_s	-0.4102	-0.4102	rad/s
σ_2	1.877×10^{-6}	2.375×10^{-6}	Nm/(rad/s)

Table 3
Coulomb plus viscous friction model parameters of the right drive mechanism.

Friction parameters	When velocity is positive	When velocity is negative	Unit
T_c	-5.6×10^{-4}	-4.561×10^{-4}	Nm
σ	1.888×10^{-6}	1.248×10^{-6}	Nm/(rad/s)

Table 4
Stribeck friction model parameters of the right drive mechanism.

Friction parameters	When velocity is positive	When velocity is negative	Unit
T_c	-5.668×10^{-4}	-4.556×10^{-4}	Nm
T_s	-4.654×10^{-4}	-4.653×10^{-4}	Nm
ν_s	-0.4102	-0.4102	rad/s
σ_2	1.876×10^{-6}	1.252×10^{-6}	Nm/(rad/s)

and the equivalent moment of inertia to the output shaft of the DC motor. In this section, practical methods of identifying the friction and the equivalent moment of inertia are proposed.

2.1. Friction parameters identification

Because of the high nonlinearity and hysteresis characteristics, precise friction modelling is very difficult, if not impossible. Many

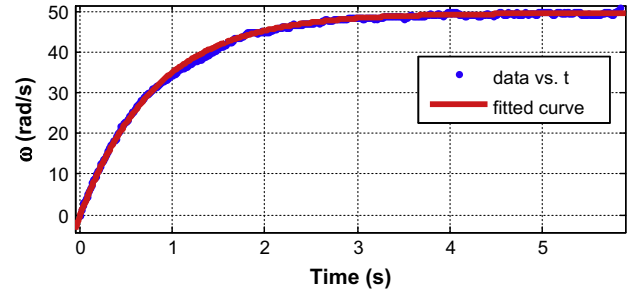


Fig. 4. Experimental velocity data of DC motor and fitting curve.

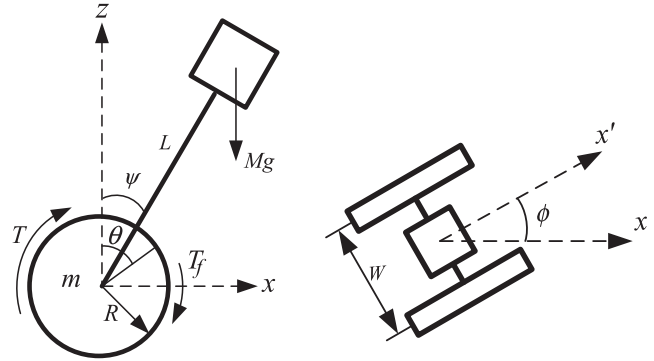


Fig. 5. Side view and top view of the robot.

friction models have been proposed to describe the behaviour of friction, such as Coulomb friction, viscous friction, Stribeck friction, the Dahl model, and the LuGre friction model. Usually, there are subtle and refined differences between these friction models. However, some of these models are much more difficult than other models. For instance, the average bristle deflection in the LuGre model can be measured directly. In this paper, Coulomb plus viscous friction and Stribeck friction are adopted to fit the practical friction contrastively because of simplicity and because they model the main behaviour of friction.

The Coulomb plus viscous friction model describes the relationship between friction and speed, which can be represented as follows [28]:

$$T_f = T_c \operatorname{sgn}(\omega) + \sigma \omega. \quad (1)$$

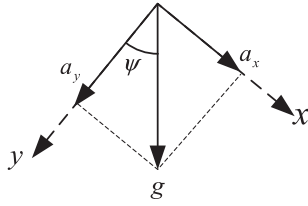


Fig. 6. Components of the gravitational acceleration.

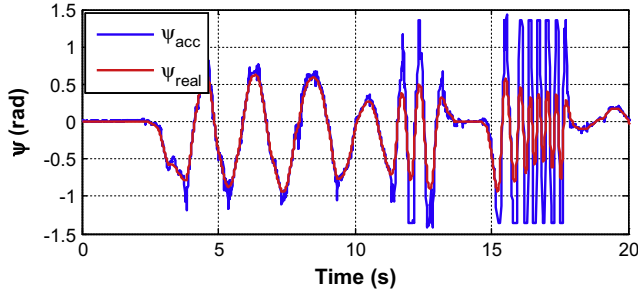


Fig. 7. Pitch angle calculated from accelerometer data and real pitch angle.

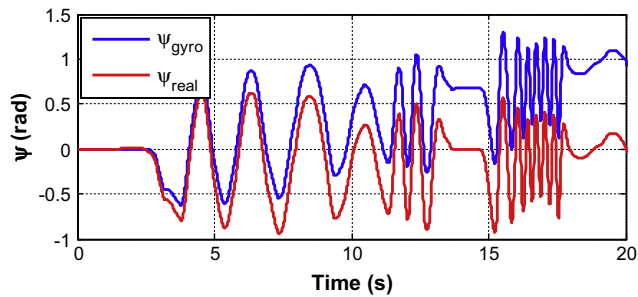


Fig. 8. Pitch angle integrated from the data of the gyro and the real pitch angle.

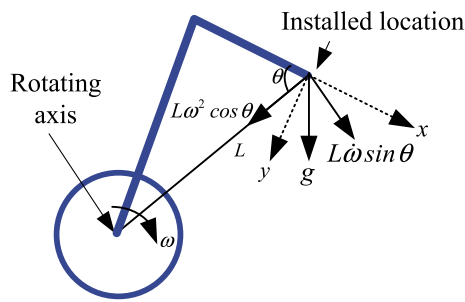


Fig. 9. Sensor installation site affects the gravitational acceleration measurement.

It should be noted that the friction torque and other parameters, such as moment of inertia, in this paper are equivalent to the output of the DC motors. In the literature, the reduction ratio of the gear box is usually taken as 1. However, it is more practical that the reduction ratio n is not equal to 1. For instance, it is 13.7 in this paper. When the reduction ratio is not equal to 1, the values of some transmission mechanism parameters are different when transformed equivalently to the output shaft of the gear box or to the motor shaft. For example, the value of the rotary inertia reflected on the motor shaft is $\frac{1}{n^2}$ of that reflected on the output shaft of the gear box. From this point of view, the modelling

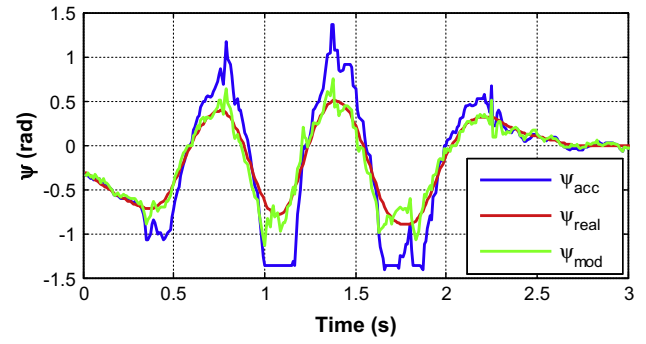


Fig. 10. Pitch angle modification of the sensor installation site.

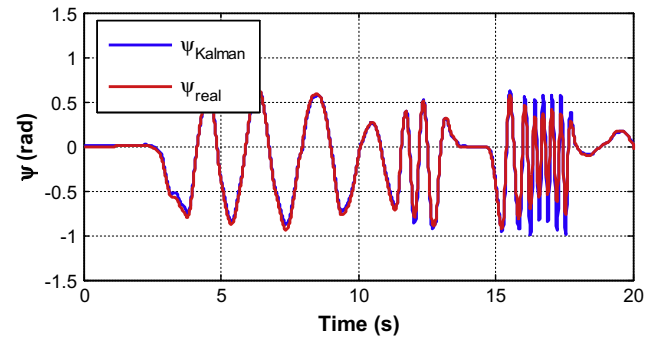


Fig. 11. Pitch angle obtained by the Kalman filter and the real pitch angle.

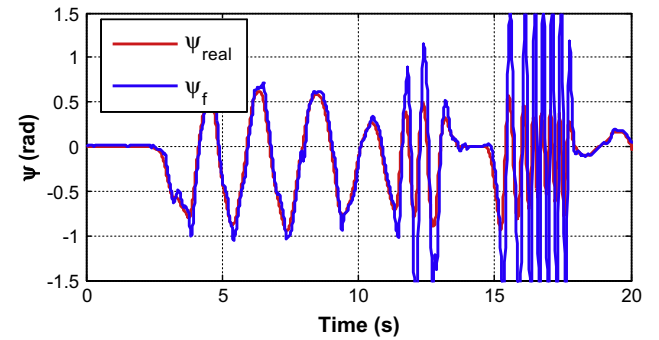


Fig. 12. Pitch angle obtained by the 2nd digital filter and the real pitch angle.

method is appropriate for the situation by dealing with the friction torque and the transmission mechanism parameters on the motor shaft.

When the motor rotates with a state velocity, the motor driving torque is equal to the friction torque because the system is in equilibrium. Because the motor driving torque is linear to the motor current, the friction torque can be obtained by measuring the motor current. The motor driving torque T_m is represented as:

$$T_m = K_t I \quad (2)$$

The experimental friction data are shown by the blue asterisk line in Fig. 2, and the green dashed line is the fitted friction by the Coulomb plus viscous friction model.

After obtaining sufficient experimental data, the MATLAB function fitting tool *cftool* is used to fit the friction model. In the Coulomb plus viscous friction model, the friction torque is linear to the rotating velocity ω when the sign of the velocity is

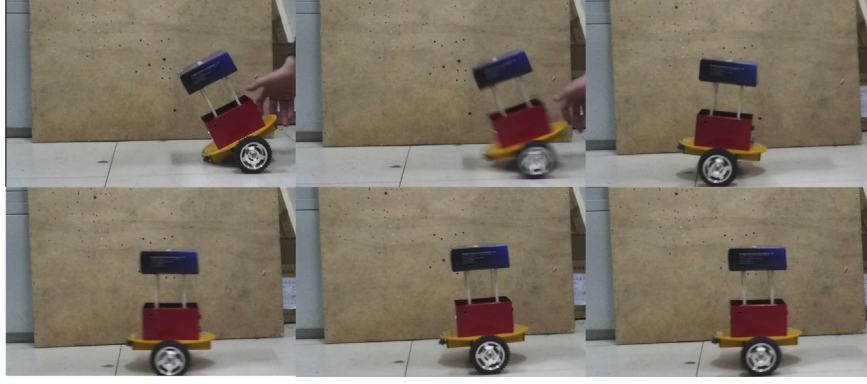


Fig. 13. Video snapshots of the balancing experiment.

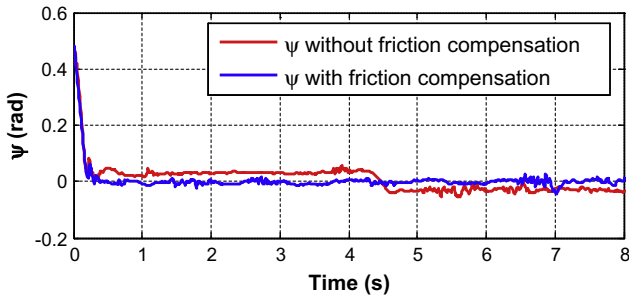


Fig. 14. Pitch angle in self-balancing movement with and without friction compensation.

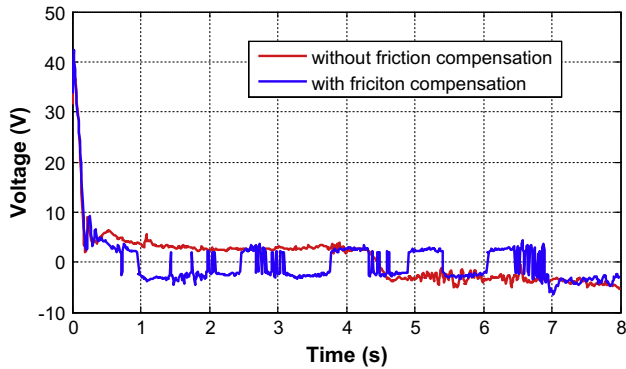


Fig. 15. Control input with and without friction compensation.

determined. Therefore, the function $y = ax + b$ is chosen as the fitting function at a positive velocity of ω , and $y = -ax + b$ is chosen at a negative velocity of ω . After importing the experimental data, *cftool* returns the coefficients a and b , and the coefficients are related to the friction parameters by:

$$\begin{cases} T_c = a \\ \sigma = b \end{cases} \quad (3)$$

From Eq. (3), the results of the friction model parameters are shown in Table 1.

The Stribeck friction model is more complex compared with the Coulomb plus viscous friction model [28], and it is represented by:

$$T_f = T_c + (T_s - T_c)e^{-\left(\frac{\omega}{v_s}\right)^2} \text{sgn}(\omega) + \sigma_2 \omega, \quad (4)$$

where $\text{sgn}(\bullet)$ is the sign function. Similar to the first friction model, the parameters of the Stribeck friction model of the left drive

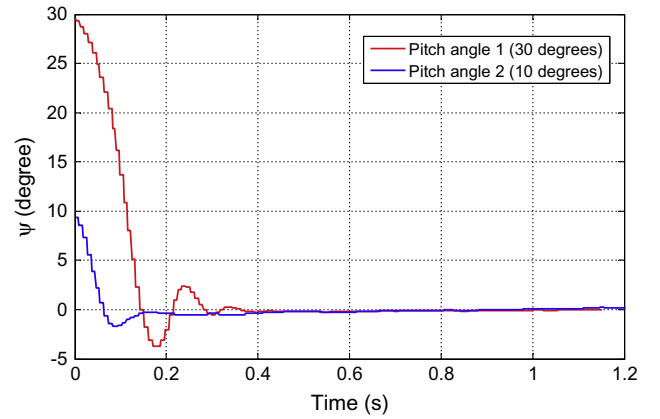


Fig. 16. Pitch angle in the balancing experiment using a PID controller.

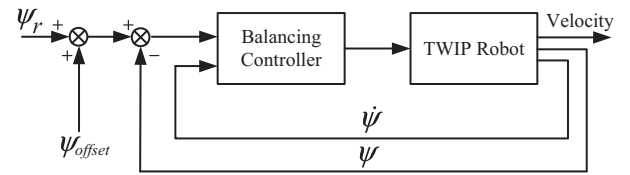


Fig. 17. Straight line movement control.

mechanism are also obtained by adopting the MATLAB function fitting tool *cftool*. For the Stribeck friction model, $y = a + be^{-\left(\frac{x}{v_s}\right)^2} + dx$ and $y = a - be^{-\left(\frac{x}{v_s}\right)^2} + dx$ are chosen as the fitting functions when the velocity is positive and negative. The Stribeck friction parameters can be obtained from the coefficients returned by *cftool* as

$$\begin{cases} T_c = a \\ T_s = a + b \\ v_s = c \\ \sigma_2 = d \end{cases} \quad (5)$$

The results are shown in Table 2.

The fitted friction curve of the Stribeck friction model is shown as a red dashed line in Fig. 2. The difference between the two friction models is tiny and hard to distinguish, and the experimental friction data are both fitted by the two models well.

Accordingly, the parameters of the two friction models of the right drive mechanism are shown in Tables 3 and 4.

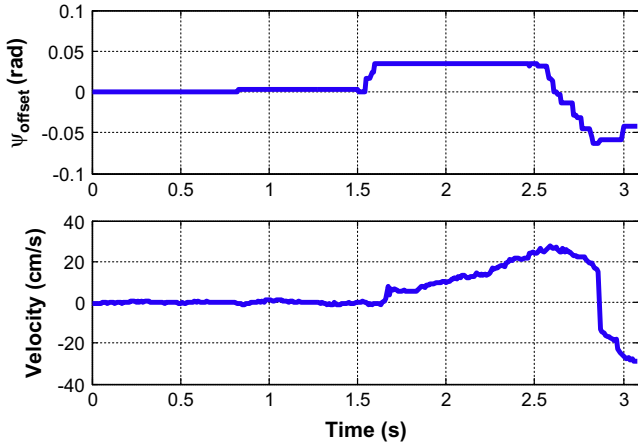


Fig. 18. Offset pitch angle and moving velocity.

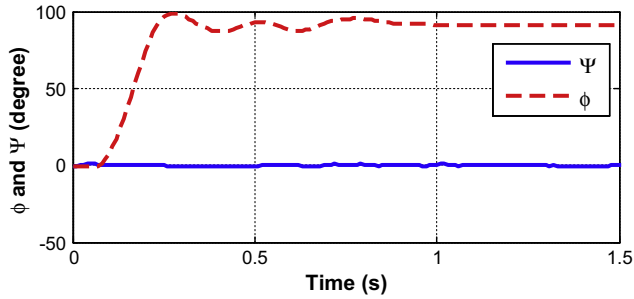


Fig. 19. Yaw movement of the TWIP robot.

The friction fitting results of the right drive mechanism are shown in Fig. 3.

In this section, the Coulomb plus viscous friction model and the Stribeck friction model are adopted to fit the friction torque of the drive mechanism. The result indicates that the differences between the two models are subtle and that both of the models fit the experimental data well. To simplify the calculation, the Coulomb plus viscous friction model is adopted in the practical friction compensation of the TWIP robot in this paper.

2.2. Identification of the equivalent moment of inertia

The rotary inertia of the wheel is commonly difficult to calculate because of the irregular shape and uneven mass distribution. In the literature, the gear ratio is usually regarded as 1 in dynamics modelling, which is not true in actuality. In this section, the rotary inertial of the wheel is equivalent to the output of the DC motor, and a novel method is identified by fitting the experimental data.

The theorem of the angular momentum of a motor rotating shaft can be expressed by

$$J\dot{\omega} = T_m - T_f. \quad (6)$$

Substituting the friction of (6) by (1), we have

$$J\dot{\omega} = T_m - (T_s + \sigma\omega). \quad (7)$$

By solving this differential equation and considering $\omega(0) = 0$, we have

$$\omega = \frac{T_m - T_s}{\sigma} - \frac{T_m - T_s}{\sigma} e^{-\frac{\sigma}{J}t}, \quad (8)$$

where the drive torque T_m produced by the motor is proportion to the current:

$$T_m = K_m i. \quad (9)$$

Eq. (8) shows that time is the only variable of the velocity ω when the drive torque is held as a state value and the parameters of friction are already identified.

An accelerating experiment is conducted when the motor current is set to a state value, for instance, 70 mA in our experiment. The velocity changing with time is shown as the blue line in Fig. 4.

Using the MATLAB function fitting tool *cftool*, the fitting curve can be obtained, shown as the red line in Fig. 4, and in the *cftool* setting, the fitting function is chosen as:

$$f(x) = a - a \times e^{-bt}. \quad (10)$$

where $a = \frac{T_m - T_s}{\sigma}$ and $b = \frac{\sigma}{J}$.

The values of a and b can be calculated by *cftool*, and the equivalent rotary inertial can be obtained as

$$J = \frac{\sigma}{b}. \quad (11)$$

To verify the method of identification of the equivalent moment of inertia proposed in this paper, the rotary inertial is also estimated. The equivalent rotary inertial includes three parts, the rotary inertial of the wheel equivalent to the motor shaft, the rotary inertial of the gear box equivalent to the motor shaft and the rotary inertial of the motor shaft itself. Based on the assumption that the wheel's mass is uniformly distributed, the total equivalent rotary inertia can be represented as:

$$J = \frac{m_w R^2}{2n^2} + J_m + J_{redu}, \quad (12)$$

The result of the estimated equivalent moment of inertia is $1.3028 \times 10^{-6} \text{ kg m}^2$, while the calculated result using the aforementioned method is $1.5450 \times 10^{-6} \text{ kg m}^2$. The two results are approximately equal to each other, which validates the proposed method.

3. Dynamics modelling

The side and top views of the robot are schematically illustrated in Fig. 5 in which the parameters of the balancing motion and yaw motion of the robot are described.

In the following paragraphs, the dynamic model of the robot is constructed based on the Lagrangian function method. Compared with existing works, the proposed dynamic model proposed in this paper is more conforming to actual situations considering drive mechanism friction and the reduction ratio.

The Lagrangian function L_a can be expressed as:

$$L_a = T_1 + T_2 + U. \quad (13)$$

Because there are three degrees of freedom, three generalized variables should be determined. The average angle of the wheel θ , the pitch angle ψ and the yaw angle ϕ are selected as the generalized variables. It should be noted that θ_l and θ_r can also be selected as generalized variables, but ϕ would be unnecessary in that situation. The average angle of the wheels θ can be defined as follows [29]:

$$\theta = \frac{1}{2}(\theta_l + \theta_r). \quad (14)$$

The yaw angle is

$$\phi = \frac{R}{W}(\theta_r - \theta_l) \quad (15)$$

The translational kinetic energy of the TWIP robot is

$$T_1 = \frac{1}{2}m(\dot{x}_l^2 + \dot{y}_l^2) + \frac{1}{2}m(\dot{x}_r^2 + \dot{y}_r^2) + \frac{1}{2}M(\dot{x}_b^2 + \dot{y}_b^2 + \dot{z}_b^2). \quad (16)$$

Similarly, the rotational kinetic energy and the potential energy of the robot can be expressed as follows:

$$T_2 = \frac{1}{2}J_w\dot{\theta}_l^2 + \frac{1}{2}J_w\dot{\theta}_r^2 + \frac{1}{2}J_\psi\dot{\psi}^2 + \frac{1}{2}J_\phi\dot{\phi}_l^2 + \frac{1}{2}n^2J_m(\dot{\theta}_l - \dot{\psi})^2 + \frac{1}{2}n^2J_m(\dot{\theta}_r - \dot{\psi})^2, \quad (17)$$

$$U = Mg z_b. \quad (18)$$

The Lagrange equations are

$$\frac{d}{dt} \left(\frac{\partial L_a}{\partial \dot{\theta}} \right) - \frac{\partial L_a}{\partial \theta} = F_\theta. \quad (19)$$

$$\frac{d}{dt} \left(\frac{\partial L_a}{\partial \dot{\psi}} \right) - \frac{\partial L_a}{\partial \psi} = F_\psi. \quad (20)$$

$$\frac{d}{dt} \left(\frac{\partial L_a}{\partial \dot{\phi}} \right) - \frac{\partial L_a}{\partial \phi} = F_\phi, \quad (21)$$

where F_θ , F_ψ , and F_ϕ are the generalized forces, and they are given by

$$F_\theta = F_l + F_r, \quad (22)$$

$$F_\psi = -F_l - F_r, \quad (23)$$

$$F_\phi = \frac{W}{2R}(F_r - F_l), \quad (24)$$

where F_l and F_r are the torques on the left and right wheel of the robot, respectively, and are represented as

$$F_l = nK_t i_l + T_s + \sigma_m(\dot{\psi} - \dot{\theta}_l), \quad (25)$$

$$F_r = nK_t i_r + T_s + \sigma_m(\dot{\psi} - \dot{\theta}_r), \quad (26)$$

where T_s and σ_m are the friction parameters identified in Section 2.

In (25) and (26), i_l and i_r are the DC motor currents that cannot be output from the controller, and they are related to the voltage and speed of the DC motor by

$$L_m \dot{i}_{l,r} = v_{l,r} + nK_b(\dot{\psi} - \dot{\theta}_{l,r}) - R_m i_{l,r}. \quad (27)$$

Usually, the motor inductance is negligible and is approximated as zero, giving

$$i_{l,r} = \frac{v_{l,r} + nK_b(\dot{\psi} - \dot{\theta}_{l,r})}{R_m}. \quad (28)$$

Substituting (25) and (26) into (28), we have

$$F_{l,r} = nK_t \frac{v_{l,r} + nK_b(\dot{\psi} - \dot{\theta}_{l,r})}{R_m} + T_s + \sigma_m(\dot{\psi} - \dot{\theta}_{l,r}), \quad (29)$$

Taken together, the robot dynamics is governed by the following differential equations:

$$\begin{aligned} &((2m + M)R^2 + 2J_w + 2n^2J_m)\ddot{\theta} + (MLR \cos \psi - 2n^2J_m)\ddot{\psi} \\ &- MLR\dot{\psi}^2 \sin \psi = F_\theta, \end{aligned} \quad (30)$$

$$\begin{aligned} &(MLR \cos \psi - 2n^2J_m)\ddot{\theta} + (ML^2 + J_\psi + 2n^2J_m)\ddot{\psi} - MgL \sin \psi \\ &- ML^2\dot{\phi}^2 \sin \psi \cos \psi = F_\psi, \end{aligned} \quad (31)$$

$$\begin{aligned} &\left(\frac{1}{2}mW^2 + J_\phi + \frac{W^2}{2R^2}(J_w + n^2J_m) + ML^2 \sin^2 \psi \right) \ddot{\phi} \\ &+ 2ML^2\dot{\psi}\dot{\phi} \sin \psi \cos \psi = F_\phi. \end{aligned} \quad (32)$$

where

$$F_\theta = \frac{nK_t}{R_m}(v_l + v_r) + 2\left(\frac{n^2K_tK_b}{R_m} + \sigma_m\right)\dot{\psi} - 2\left(\frac{n^2K_tK_b}{R_m} + \sigma_m\right)\dot{\theta} + 2T_s, \quad (33)$$

$$F_\psi = -\frac{nK_t}{R_m}(v_l + v_r) - 2\left(\frac{n^2K_tK_b}{R_m} + \sigma_m\right)\dot{\psi} + 2\left(\frac{n^2K_tK_b}{R_m} + \sigma_m\right)\dot{\theta} - 2T_s, \quad (34)$$

$$F_\phi = \frac{nK_tW}{2RR_m}(v_r - v_l) - \frac{W^2}{2R^2}\left(\frac{n^2K_tK_b}{2R_m} + \sigma_m\right)\dot{\phi}. \quad (35)$$

Eqs. (33)–(35) can be rewritten as state equations based on modern control theory and selecting state variables as

$$\begin{cases} x_1 = \theta \\ x_2 = \dot{\theta} \\ x_3 = \psi \\ x_4 = \dot{\psi} \\ x_5 = \phi \\ x_6 = \dot{\phi} \end{cases}. \quad (36)$$

We have

$$M(x)\dot{x} = f(x) + u, \quad (37)$$

where

$$M(x) = \begin{bmatrix} 1 & 0 & 0 & 0 & 0 & 0 \\ M_{21} & M_{22} & -M_{21} & M_{24} & 0 & 0 \\ 0 & 0 & 1 & 0 & 0 & 0 \\ -M_{21} & M_{24} & M_{21} & M_{44} & 0 & 0 \\ 0 & 0 & 0 & 0 & 1 & 0 \\ 0 & 0 & 0 & 0 & M_{65} & M_{66} \end{bmatrix}, \quad (38)$$

$$f(x) = \begin{bmatrix} f_1 \\ f_2 \\ f_3 \\ f_4 \\ f_5 \\ f_6 \end{bmatrix} = \begin{bmatrix} x_2 \\ MLRx_4^2 \sin x_3 + 2T_s \\ x_4 \\ MgL \sin x_3 + ML^2x_6^2 \sin x_3 \cos x_3 \\ x_6 \\ -2ML^2x_4x_6 \sin x_3 \cos x_3 \end{bmatrix}, \quad (39)$$

$$u = \begin{bmatrix} 0 \\ u_2 \\ 0 \\ -u_2 \\ 0 \\ u_6 \end{bmatrix} = \begin{bmatrix} 0 & 0 \\ \frac{nK_t}{R_m} & \frac{nK_t}{R_m} \\ 0 & 0 \\ -\frac{nK_t}{R_m} & -\frac{nK_t}{R_m} \\ 0 & 0 \\ \frac{nK_tW}{2RR_m} & -\frac{nK_tW}{2RR_m} \end{bmatrix} \begin{bmatrix} v_r \\ v_l \end{bmatrix}. \quad (40)$$

It should be noted that u is the input of the controller, which can be determined by the controller.

4. Sensor data fusion

The precise pitch angle measurement is crucial to the TWIP robot because it is the foundation for balancing control. In this section, different methods to calculate the pitch angle information are discussed, and a low cost estimating method considering the

installation site of sensors is proposed, which fuses the data from the gyro and accelerometer based on a Kalman filter.

4.1. Estimating method with a single accelerometer

The gravitational acceleration is always vertical to the horizontal surface. Thus, the pitch angle ψ can be achieved by measuring the component of the gravitational acceleration along the coordinate axes fixed on the robot body.

As illustrated in Fig. 6, the x -axis and y -axis are the axes of the coordinate fixed on the robot body, and a_x and a_y are the components of the gravitational acceleration along the x -axis and y -axis, respectively. From Fig. 6, we have

$$\psi = \arcsin\left(\frac{a_x}{g}\right) \text{ or } \psi = \arctan\left(\frac{a_x}{a_y}\right). \quad (41)$$

However, (41) is only a theoretical calculation equation, which cannot be adopted directly because a_x and a_y are difficult to measure precisely. The accelerometer is sensitive to any acceleration, not only the component of gravitational acceleration, and the measurement result of the accelerometer is easily influenced by the robot body's vibration. Another notable factor is the high price of the high-accuracy accelerometer.

The pitch angle calculated from accelerometer data ψ_{acc} and the real pitch angle ψ_{real} are compared in Fig. 7. The real pitch angle ψ_{real} was measured by a photoelectric rotary encoder installed on the DC motor. Specifically, the robot became a simple inverted pendulum when the two wheels were fixed. The rotary angle of the encoder was the pitch angle. In this situation, the wheels of the robot were fixed. Thus, the robot became a simple inverted pendulum, and the rotary angle of the encoder was the pitch angle.

Fig. 7 shows that ψ_{acc} is close to ψ_{real} when the pitch angle varies slowly. However, the amplitude of ψ_{acc} is not close to ψ_{real} when the pitch angle changes quickly. This phenomenon occurs because the quickly changing pitch angle usually causes oscillation of the robot body. It can be concluded that the estimated method using a single accelerometer is only suitable when the pitch angle is constant or varies slowly. Another notable phenomenon is that the phases of ψ_{acc} are almost the same as those of ψ_{real} , which is different from the output from an analogue or digital filter.

4.2. Estimating method with a single gyro

Because the pitch angle rate $\dot{\psi}$ can be measured by a gyro, the pitch angle can be obtained by integrating the pitch angle rate against time, as

$$\psi_{k+1} = \psi_k + \dot{\psi} \times \Delta t. \quad (42)$$

However, this method also has a serious drawback that the estimation error increases over time because of gyro drift. As time elapsed, the pitch angle obtained by this method became seriously distorted and could not be used. The phenomenon is shown in Fig. 8 in which we can find that the pitch angle integrated from the data of the gyro is accurate only in the short term but not over a long period.

4.3. Acceleration measurement modification of the sensor installation site

As mentioned in sub-section A, the acceleration caused by the oscillation of the robot body would deteriorate the measurement of the gravitational acceleration component. To obtain a precise pitch angle, the sensor installation site is an important factor that should be accounted for, but it is rarely discussed in the literature. Because of limitations in space or for convenience, the sensor used

in the TWIP robot is usually not installed on the rotary axis of the robot. For instance, the sensor installation site in Fig. 9 is a distance L from the rotary axis of the wheel, and the connection line of the sensor installation site and the rotary axis of the wheel makes an angle θ with the installed plane of the sensor.

As shown in Fig. 9, the acceleration along the x -axis and y -axis will be different from that illustrated in Fig. 6 for the rotation of the robot body. The impact to a_x and a_y of the sensor installation site and the robot body rotation can be expressed as

$$a_x = g \sin \psi - L\omega^2 \cos \theta + L\dot{\omega} \sin \theta, \quad (43)$$

$$a_y = g \cos \psi + L\omega^2 \sin \theta + L\dot{\omega} \cos \theta. \quad (44)$$

The measurement result of the accelerometer can be modified according to (43) and (44). The result of the modification is illustrated in Fig. 10. ψ_{acc} is the pitch angle directly calculated from the acceleration measured by the accelerometer, ψ_{mod} is the pitch angle calculated from the modified acceleration according to (43) and (44), and ψ_{real} is the real pitch angle. This figure shows that the modification is significant and necessary.

4.4. Multi-sensor data fusion based on a Kalman filter

A Kalman filter is an effective tool to process noisy sensor data, especially to fuse multi-sensor data associated with each other [17]. Using the modified acceleration obtained in sub-section C and the angle rate from the gyro as the input of the Kalman filter, the pitch angle is estimated.

The filtered pitch angle is shown in Fig. 11, where ψ_{Kalman} is the pitch angle fused by the Kalman filter and ψ_{real} is the real pitch angle.

For comparison purposes, the pitch angle filtered by a 2nd-order digital filter is illustrated in Fig. 12, and the bandwidth of this filter is 5 Hz. Figs. 11 and 12 demonstrate the advantages of the method proposed in this paper, even when the pitch angle of the robot changes very quickly.

5. Controller design and experiments

5.1. Sliding mode controller design

To control the TWIP robot, the sliding mode controllers for self-balancing and yaw motion are designed in this section. Although the TWIP robot is a tight coupling nonlinear system, the two controllers are designed independently and are proven to be feasible by experiments.

The sliding surface of the self-balancing controller is selected as

$$s_1 = c_1 \psi + c_2 \dot{\psi}, \quad (45)$$

where c_1 and c_2 are constants to be determined.

To make the system trajectories reach the sliding surface, the derivation of s_1 is designed as

$$\dot{s}_1 = -\varepsilon_1 \text{sgn}(s_1), \quad (46)$$

where ε_1 is a constant to be determined.

From (45) and (46), we have

$$c_1 \dot{\psi} + c_2 \ddot{\psi} = -\varepsilon_1 \text{sgn}(s_1). \quad (47)$$

From the robot dynamic Eq. (37), we have

$$M_{21}(M_{24} + M_{22})\ddot{\theta} - M_{21}(M_{24} + M_{22})\dot{\psi} + (M_{24}^2 - M_{22}M_{44})\ddot{\psi} = M_{24}f_2 - M_{22}f_4 + (M_{24} + M_{22})u_2. \quad (48)$$

Substituting $\ddot{\psi}$ in (47) with (48), we have

$$u_2 = \frac{c_2 M_{21} (M_{24} + M_{22}) \dot{\psi} - c_2 M_{21} (M_{24} + M_{22}) \dot{\psi}}{c_2 (M_{24} + M_{22})} - \frac{c_1 (M_{24}^2 - M_{22} M_{44}) \dot{\psi} + (M_{24}^2 - M_{22} M_{44}) \varepsilon_1 \operatorname{sgn}(s_1)}{c_2 (M_{24} + M_{22})} - \frac{c_2 M_{24} f_2 - c_2 M_{22} f_4}{c_2 (M_{24} + M_{22})} \quad (49)$$

Similarly, the sliding surface of the yaw motion controller is selected as

$$s_2 = c_3 \phi + c_4 \dot{\phi} \quad (50)$$

From (37) and (50), we have

$$u_6 = (M_{65} - c_3 M_{66}) \dot{\phi} - \frac{M_{66} \varepsilon_2 \operatorname{sgn}(s_2)}{c_4} - f_6 \quad (51)$$

Considering (40), (49) and (51), the voltage of the DC motors as the final control output can be obtained:

$$v_r = \frac{R R_M}{n K_t W} u_6 - \frac{R_M}{2 n K_t} u_2, \quad (52)$$

$$v_l = -\frac{R R_M}{n K_t W} u_6 - \frac{R_M}{2 n K_t} u_2. \quad (53)$$

5.2. Stability analysis

In fact, the dynamics Eq. (48) is the nominal model that cannot describe all of the details. The real system with parameter uncertainties is assumed as

$$M_{21} (M_{24} + M_{22}) \ddot{\psi} - M_{21} (M_{24} + M_{22}) \dot{\psi} + (M_{24}^2 - M_{22} M_{44}) \ddot{\psi} = M_{24} f_2 - M_{22} f_4 + (M_{24} + M_{22}) u_2 + (M_{24}^2 - M_{22} M_{44}) \Delta_1. \quad (54)$$

where Δ_1 is the parameter uncertainty.

A Lyapunov function candidate is chosen as

$$V_1 = \frac{1}{2} s_1^2. \quad (55)$$

Differentiating V_1 with respect to time, we have

$$\dot{V}_1 = -s_1 \dot{s}_1. \quad (56)$$

Considering (46), (47), (54), and the controller (49) and (56) can be rewritten as

$$\dot{V}_1 = -s_1 (\varepsilon_1 \operatorname{sgn}(s_1) + c_2 \Delta_1). \quad (57)$$

From (57), it can be found that

$$\text{if } \varepsilon_1 > c_2 \Delta_1 \text{ then } \dot{V}_1 < 0. \quad (58)$$

Then, the proposed controller (49) guarantees that the pitch angle ψ can converge to zero.

Similar to (54), the dynamic equation of the robot yaw motion is assumed as

$$M_{65} \ddot{\phi} + M_{66} \ddot{\phi} = f_6 + u_6 + M_{66} \Delta_2. \quad (59)$$

where Δ_2 is the parameter uncertainty.

Choosing the following function as a Lyapunov function candidate:

$$V_2 = \frac{1}{2} s_2^2. \quad (60)$$

Differentiating V_2 with respect to time, we have

$$\dot{V}_2 = -s_2 \dot{s}_2. \quad (61)$$

Substituting (61) into (50), (51) and (59), the derivative of V_2 can be represented as

$$\dot{V}_2 = -s_2 (-\varepsilon_2 \operatorname{sgn}(s_2) + c_4 \Delta_2). \quad (62)$$

From (62), if ε_2 is chosen to satisfy the condition

$$\varepsilon_2 > c_4 \Delta_2, \quad (63)$$

the derivative of V_2 would be negative and the yaw motion would be asymptotically stable.

5.3. Experiments

To validate the design and controllers of the TWIP robot, several experiments were conducted, including a balancing experiment, a straight line experiment and a yaw experiment.

5.3.1. Balancing experiments

Firstly, the robot was powered off and placed on the ground with a large pitch angle ($\psi = 27^\circ$). Then, the power button was switched on, and the robot stood up and maintained its balance. In Fig. 13, some video snapshots of this experiment show the progress of the robot standing up and finally maintaining its balance.

For comparison, the balancing experiments of the TWIP robot were carried out with and without friction compensation, and the results are shown in Figs. 14 and 15.

Fig. 14 shows that the friction compensation proposed in this paper can improve the steady state error effectively (approximately $2\text{--}3^\circ$). Furthermore, when friction is not compensated for, there is a crawling phenomenon, as shown in Fig. 14, at approximately 4.5 s, which is beneficial to the robot's stability.

To compare the effect of the method proposed in this paper, the classical PID controller is adopted in the balancing experiments. The transfer function of the PID controller is

$$G(s) = k_p + k_i \frac{1}{s} + k_d s, \quad (64)$$

where k_p , k_i and k_d are the proportion gain, the integral gain and the differential gain, respectively.

The results are shown in Fig. 16, where the robot recovered its balance from two initial pitch angles, 10° and 30° . The figure shows that a larger pitch angle will cause more serious overshooting when using a PID controller. Furthermore, adjusting the PID controller parameters is very difficult to obtain a satisfying performance.

5.3.2. Straight line moving experiment

As self-balancing of the TWIP robot is achieved, straight line movement can be easily implemented by adding an offset angle to the reference angle of the balancing controller. The offset angle is set by the operator via a remote device, and with a larger offset angle, the TWIP robot will move faster. The control block diagram is shown in Fig. 17, where ψ_{offset} is the offset angle and ψ_r is the reference angle (ψ_r is usually zero when the TWIP robot stays balanced).

The experimental result of the straight line movement control is shown in Fig. 18. From approximately 1.5 s, the offset pitch angle ψ_{offset} was changed by the operator. As a result, the robot started to move forward and backward. This figure shows that the TWIP robot is able to move by adding an offset angle to the reference pitch angle of the balancing controller. It should be noted that the factors affecting the velocity include not only the pitch angle but also something else, such as terrain. Little lumps and bumps on the ground will change the velocity accompanying the effect of the pitch angle, and this phenomenon can be found at approximately 2.8 s.

5.3.3. Yaw experiment

To check the steering capacity of the robot, a yaw experiment was carried out. The robot was controlled to turn a 90° angle while maintaining its balance on flat ground. The result is illustrated in Fig. 19, where the robot shows good steering ability and the yaw movement has almost no effect on the pitch angle of the robot.

6. Conclusion

In this paper, a low cost two-wheeled inverted pendulum robot with friction compensation is presented. Using a Kalman filter and considering the influence of sensor installation location on the robot body, a low cost accelerometer and gyro were implemented but achieved high performance. The parameters of the robot were identified by a novel method proposed in this paper, and the transmission mechanism friction was compensated for based on the identified friction method. Two sliding mode controllers for balancing and steering movement were designed based on the dynamic model derived by the Lagrangian function method. Finally, physical experiments were carried out and validated the effectiveness of the design of the robot, the signal processing method, the design of the controller and the friction compensation method proposed in this paper.

Acknowledgements

The author would like to thank all of the reviewers for their valuable comments.

This research has been partially supported by the National Natural Science Foundation of China (Grant No. 61273344), the Ph.D. Program Foundation of the Ministry of Education of China (Grant No. 20121101110011), the State Key Laboratory of Robotics and Systems (HIT) (Grant No. SKLRS-2011-ZD-06) and the National Hi-tech Research and Development Program of China (Grant 2008AA04Z208).

References

- [1] Tsui KM, Desai M, Yanco HA, Uhlik C. Exploring use cases for telepresence robots. *ACM/IEEE Int Conf HRI* 2011;11–8.
- [2] Ravichandran MT, Mahindrakar AD. Robust stabilization of a class of underactuated mechanical systems using time scaling and lyapunov redesign. *IEEE Trans Ind Electron* 2011;58(9):4299–313.
- [3] Shui-Chun L, Ching-Chih T. Development of a self-balancing human transportation vehicle for the teaching of feedback control. *IEEE Trans Educ* 2009;52(1):157–68.
- [4] Lee J, Shin H, Lee S, Jung S. Balancing control of a single-wheel inverted pendulum system using air blowers: evolution of mechatronics capstone design. *Mechatronics* 2012;23(8):926–32.
- [5] Nakagawa C, Nakano K, Suda Y, Hayashi R. Stability of the dynamically stabilized two-wheeled vehicle traveling on a rough road. *J Mech Syst Trans Logis* 2009;2:78–89.
- [6] Solis J, Nakadate R, Yoshimura Y, Hama Y, Takanishi A. Development of the two-wheeled inverted pendulum type mobile robot WV-2R for educational purposes. *IEEE IROS* 2009:2347–52.
- [7] Grasser F, D'Arrigo A, Colombi S, Rufer AC. JOE: a mobile, inverted pendulum. *IEEE Trans Ind Electron* 2002;49(1):107–14.
- [8] Guo Z-Q, Xu J-X, Heng Lee T. Design and implementation of a new sliding mode controller on an underactuated wheeled inverted pendulum. *J Franklin Inst* 2013;16–32.
- [9] Huang J, Ding F, Fukuda T, Matsuno T. Modeling and velocity control for a novel narrow vehicle based on mobile wheeled inverted pendulum. *IEEE Trans Control Syst Technol* 2013;21(5):1607–17.
- [10] Chaoquan L, Xueshan G, Qiang H, Fuquan D, Jie S, Yang B, et al. A coaxial couple wheeled robot with T-S fuzzy equilibrium control. *Ind Robot* 2011;38(3):292–300.
- [11] Xu J, Guo Z, Lee T. Design and implementation of a Takagi-Sugeno type fuzzy logic controller on a two-wheeled mobile robot. *IEEE Trans Ind Electron* 2013;60(12):5717–28.
- [12] Chiu C-H, Chang C-C. Design and development of Mamdani-like fuzzy control algorithm for a wheeled human-conveyance vehicle control. *IEEE Trans Ind Electron* 2012;59(12):4774–83.
- [13] Li Z, Yang C. Neural-adaptive output feedback control of a class of transportation vehicles based on wheeled inverted pendulum models. *IEEE Trans Control Syst Technol* 2012;20(6):1583–91.
- [14] Chiu C-H, Lin Y-W, Lin C-H. Real-time control of a wheeled inverted pendulum based on an intelligent model free controller. *Mechatronics* 2011;21(3):523–33.
- [15] Sun Z, Ge S, Lee T. Stabilization of underactuated mechanical systems: a non-regular back-stepping approach. *Int J Control* 2001;74(11):1045–51.
- [16] Hu J-S, Tsai M-C, Hu F-R, Hori Y. Robust control for coaxial two-wheeled electric vehicle. *J Mar Sci Technol* 2010;18(2):172–80.
- [17] Shui-Chun L, Ching-Chih T, Hsu-Chih H. Adaptive robust self-balancing and steering of a two-wheeled human transportation vehicle. *J Intell Robot Syst* 2011;62(1):103–23.
- [18] Lee H, Jung S. Balancing and navigation control of a mobile inverted pendulum robot using sensor fusion of low cost sensors. *Mechatronics* 2012;22(1):95–105.
- [19] Gomez M, Arribas T, Sanchez S. Optimal control based on CACM-RL in a two-wheeled inverted pendulum. *Int J Adv Rob Sys* 2012:9.
- [20] Abdullah Bin Azhar M, Hassan W, Rahim U. PID control behavior and sensor filtering for a self balancing personal vehicle. *IEEE ICRAI* 2012:7–10.
- [21] Voth D. Segway to the future. *IEEE Intell Syst* 2005;20(3):5–8.
- [22] Olsson H, Astrom KJ, Canudas de Wit C, Gafvert M, Lischinsky P. Friction models and friction compensation. *Eur J Control* 1998;4(3):176–95.
- [23] Shang W, Cong S, Zhang Y. Nonlinear friction compensation of a 2-DOF planar parallel manipulator. *Mechatronics* 2008;18(7):340–6.
- [24] Rizzo DD, Fasseis SD. Friction identification based upon the LuGre and Maxwell slip models. *IEEE Trans Control Syst Technol* 2009;17(1):153–60.
- [25] Uzun L, Salásek J. HOSIDF-based feedforward friction compensation in low-velocity motion control systems. *Mechatronics* 2014;24(2):118–27.
- [26] Márton L, Fodor S, Sepehri N. A practical method for friction identification in hydraulic actuators. *Mechatronics* 2011;21(1):350–6.
- [27] Sunan H, Kok-Kiong T. Intelligent friction modeling and compensation using neural network approximations. *IEEE Trans Ind Electron* 2012;59(8):3342–9.
- [28] Bona B, Indri M. Friction compensation in robotics: an overview. In: *Decision and control, 2005 and 2005 european control conference. CDC-ECC'05. 44th IEEE Conference on*; 2005. p. 4360–7.
- [29] Chaoquan L. Study on the coaxial two-wheeled robot and the equilibrium control technologies [D]. Beijing Institute of Technology; 2011.